Journal of Power Sources 633 (2025) 236363

Contents lists available at ScienceDirect

Journal of Power Sources

journal homepage: www.elsevier.com/locate/jpowsour

# Modelling thermal runaway of cylindrical battery under sub-atmospheric pressure

Yanhui Liu [a,b,1], Changxiang He [c,1], Gregory Offer [b], Huizhi Wang [b,**], Xinyan Huang [a,*], Tianshou Zhao [c,d]

[a] Department of Building Environment and Energy Engineering, The Hong Kong Polytechnic University, Hong Kong Special Administrative Region of China
[b] Department of Mechanical Engineering, Imperial College London, London, United Kingdom
[c] Department of Mechanical and Aerospace Engineering, The Hong Kong University of Science and Technology, Hong Kong Special Administrative Region of China
[d] Department of Mechanical and Energy Engineering, Southern University of Science and Technology, Shenzhen, China

## HIGHLIGHTS

- A numerical model simulates battery thermal runaway under sub-atmospheric pressure.
- Analyse the impact of safety valve threshold on battery internal pressure evolution.
- Quantify pressure and gas composition from SEI decomposition at the venting point.
- Examine coupled ambient-pressure effect of cell heating rate and convective cooling.

## GRAPHICAL ABSTRACT

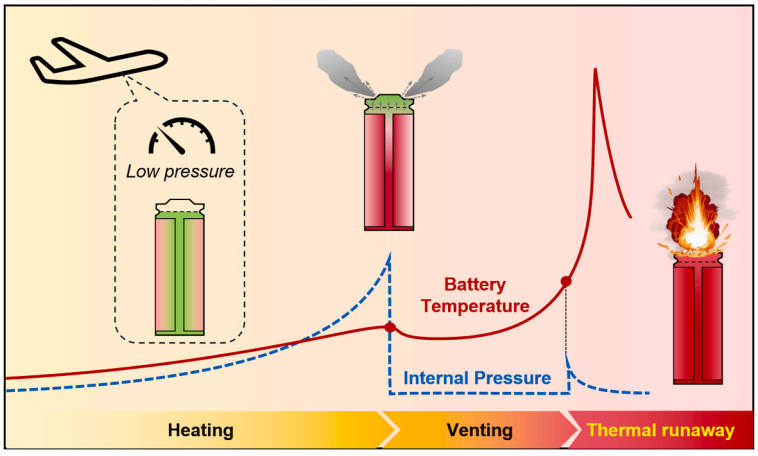


## ARTICLE INFO

*Keywords:*
Battery safety
Low ambient pressure
Venting
Cell pressure
Numerical simulation

## ABSTRACT

The storage and transportation of lithium-ion batteries under reduced ambient pressure have critical safety concerns. This work develops a model to simulate and understand the thermal runaway of a cylindrical battery cell at different sub-atmospheric pressures. A lumped heat transfer model for batteries is upgraded by considering the increasing electrolyte loss observed in experiments as pressure decreases. Using the model, we examine the impacts of ambient pressure, cell heating rate, and safety-venting threshold on battery thermal failure, with a particular focus on safety venting and thermal runaway. Before safety venting, the internal cell pressure is raised initially by electrolyte vaporisation and then by gases produced from chemical reactions. As the safety valve

* Corresponding author.
** Corresponding author.
*E-mail addresses:* yanhui2021.liu@connect.polyu.hk (Y. Liu), cheag@connect.ust.hk (C. He), gregory.offer@imperial.ac.uk (G. Offer), huizhi.wang@imperial.ac.uk (H. Wang), xy.huang@polyu.edu.hk (X. Huang), zhaots@sustech.edu.cn (T. Zhao).
[1] Joint first author, these authors contributed equally to this study.

https://doi.org/10.1016/j.jpowsour.2025.236363
Received 31 August 2024; Received in revised form 12 January 2025; Accepted 25 January 2025
Available online 6 February 2025
0378-7753/Crown Copyright © 2025 Published by Elsevier B.V. This is an open access article under the CC BY-NC license (http://creativecommons.org/licenses/by-nc/4.0/).

threshold rises from 1.2 MPa to 2.2 MPa, the gas from SEI decomposition increases from 73.5 % to 82.3 % at the moment of safety venting. The incubation period between venting and thermal runaway increases as the ambient pressure decreases. In other words, lowering the ambient pressure allows more emergency response time before thermal runaway. The developed model approach and simulations improve our understanding of thermal runaway under low ambient pressures and provide novel insights for ensuring battery safety in storage and transportation.

Nomenclature

| Symbols | | Subscripts | |
|---|---|---|---|
| $A$ | surface area ($m^2$) | *cr* | critical |
| $E$ | activation energy (J $mol^{-1}$) | *ele* | electrolyte |
| $h$ | heat transfer coefficient (W $m^{-2}$ $K^{-1}$) | *ex* | external |
| $\Delta H$ | heat of reactions (kJ $kg^{-1}$) | *g* | gas |
| $m$ | mass (g) | *in* | internal |
| $M$ | molecular mass (g $mol^{-1}$) | *max* | maximum |
| $n$ | gas amount (mol) | *TR* | thermal runaway |
| $P$ | pressure (kPa) | *v* | safety venting |
| $\dot{q}$ | heating/cooling rate (kW) | *0* | initial value |
| $R$ | universal gas constant (J $mol^{-1}$ $K^{-1}$) | **Abbreviations** | |
| $t$ | time (s) | *CFD* | computational fluid dynamics |
| $\Delta t$ | time interval (s) | *DMC* | dimethyl carbonate |
| $T$ | temperature (°C) | *EC* | ethylene carbonate |
| $\dot{T}$ | temperature rise rate (°C $min^{-1}$) | *EDS* | energy dispersive spectrometer |
| $V$ | volume ($m^3$) | *EMC* | ethyl methyl carbonate |
| $Z$ | pre-exponential factor ($s^{-1}$) | *ISC* | internal short circuit |
| | | *LCO* | lithium cobalt oxide |
| ***Greeks*** | | *LIB* | lithium-ion battery |
| $\alpha$ | non-dimensional amount for reactants | *NCM* | lithium nickel manganese cobalt oxides |
| $\delta$ | partial pressure ratio | *ODE* | ordinary differential equation |
| $\eta$ | effective mass loss fraction | *SEI* | solid electrolyte interface |

## 1. Introduction

Battery energy storage systems are crucial in the transition to more sustainable transportation and a resilient electric infrastructure [1]. Today, Li-ion batteries serve as the primary power source for electric vehicles, providing a cleaner alternative to internal combustion engines and thereby reducing emissions [2]. Additionally, batteries are essential for addressing intermittent renewable energy generation, such as solar and wind power [3]. They stabilise the integration of renewable energy into the grid by storing excess energy produced during periods of high production and releasing it when production is low [4]. However, the fire risks of batteries have become more apparent with the increasing market demand.

In civil aviation, ensuring battery fire safety under low ambient pressure has been a significant issue [5]. Despite the requirement set by UN T 38.3 that battery packs must undergo a low-pressure storage test at 11.6 kPa for a minimum of 6 h, incidents of battery fires under low-pressure conditions continue to occur [6]. Federal Aviation Administration (FAA) reports that over 540 battery safety incidents in air transport before July 2024. For instance, Li-ion batteries transported by FedEx ignited the plane during a flight from Memphis to Paris in 2004 (Fig. 1a). Similarly, a UPS cargo plane suffered damage from a battery fire in 2006 (Fig. 1b), resulting in the tragic deaths of two crew members. In 2013, the auxiliary power unit of a Boeing 787 caught fire, with firefighters taking 80 min to address it after the aircraft made an emergency landing (Fig. 1c). Such battery air incidents have become increasingly frequent in recent years. Between 2021 and 2023, over 200 battery fires were reported, approximately 1.5 times the number recorded from 2018 to 2020 [7]. Therefore, it is important to advance our understanding of battery fire safety under low ambient pressure.

Thermal runaway is the major concern for battery fire hazards [10], which refers to a rapid and uncontrolled temperature increase driven by a sequence of self-heating reactions [11–13]. These reactions mainly contain the solid electrolyte interface (SEI) decomposition, anode–electrolyte reaction, electrolyte decomposition, and redox reactions related to electrode materials [14]. Besides, there are also some endothermic reactions inside the battery cells, including the melting of separators and electrode collectors [15]. The separator collapse will cause an internal short circuit (ISC), which will also contribute to the joule heat during the thermal runaway process. The SEI decomposition is the beginning of battery self-heating [16], which can be initiated from 70 °C to 120 °C and release gases such as $C_2H_4$, $CO_2$, and $O_2$ [17]. The reaction between anode and electrolyte starts at about 120 °C and often releases flammable hydrocarbons such as $C_2H_4$, $C_3H_6$ and $C_2H_6$ [18,19]. This reaction can contribute significantly to heat generation and trigger thermal runaway [20]. The occurrence of thermal runaway quickly triggers redox reactions between the cathode and anode, releasing large amounts of heat and flammable gases [21]. These reactions determine the maximum temperature ($T_{max}$) that the battery can reach during thermal runaway.

Due to the installation of safety valves in cylindrical and prismatic cells, there are two distinct jet-flow events during the thermal runaway process [22–24]. Fig. 2 illustrates the temperature and internal pressure response for a cylindrical battery cell exposed to external overheating conditions [25]. At the heating phase, the originally solid jellyroll structure in the cell becomes loose and porous due to gas generation. The primary gas components inside the battery cell are from SEI decomposition, anode-electrolyte reactions, and the electrolyte vapour. These reactions gradually increase the battery temperature, and the gases cause the internal pressure of the battery cell to rise. When the internal and ambient pressure difference reaches a certain threshold, the safety valve opens, initiating the first jet event. The jet of high-temperature multiphase materials through the safety valve carries away some heat, causing a slight temperature decrease. After the safety valve opens, the cell undergoes a venting process where the internal reactions continue to raise the battery temperature, and the gaseous products, along with electrolyte vapour, volatilise from the porous materials [26]. Once the




**Fig. 1.** Photographs of the battery air incidents that happened in (a) the FedEx plane, (b) the UPS cargo plane, and (c) the Boeing 787 [8,9].

battery temperature rises to the thermal runaway initiation temperature ($T_{TR}$), a large amount of heat and flammable gases are rapidly released in a short period, leading to a second jet event [27–29].

The time interval between the safety valve opening and the thermal runaway is known as the incubation period (Fig. 2), which determines whether thermal runaway events will cascade and escalate. Such a venting period can be used to warn against thermal runaway [31,32] or implement mitigation strategies [30]. Thus, numerous researchers have studied the venting behaviours and incubation period at standard atmospheric pressure [31–35]. For example, Qin et al. [31] introduced a novel approach to separate the pressure increase caused by electrolyte vapour from that generated by gases before venting. García et al. [32] employed high-speed cameras and optical techniques to capture the behaviours of electrolyte droplets and generated gases during the venting process. Recently, Wang et al. [33] utilised planar laser scattering methods to observe the ejected particles and droplets during the venting event. Moreover, the venting process is greatly influenced by ambient pressure, which subsequently affects the initiation of thermal runaway. According to our previous findings [36,37], low ambient pressure can accelerate the evaporation and volatilisation of electrolytes after the safety valve opening, thus prolonging the incubation period and delaying thermal runaway. The delay of thermal runaway under low ambient pressure has been reported in numerous studies [38,39]. However, all the above studies investigate thermal runaway characteristics at low ambient pressure through experimental approaches. The literature lacks the numerical models to examine the evolution of thermal runaway under such conditions.

Modelling the venting and thermal runaway processes at normal ambient pressure has been a hot topic in recent years [40–46]. Table 1 summarises developments in venting models in the literature. With the advantages of high computational speed and accuracy, the lumped model is extensively used to address thermal abuse reactions and gas generation. To explore the jet dynamics as well as the distribution of gases and particles vented from the cell, the computational fluid dynamics (CFD) model is further coupled. These models propose a systematic framework to numerically study gas generation, internal pressure buildup, venting dynamics, and flaming combustion. As mentioned above, existing models mainly concentrate on simulating venting behaviours at standard atmospheric pressure. Few modelling studies have considered the influence of ambient pressure on energy dissipation and mass loss after safety valve opening, and even fewer have focused on the thermal runaway of batteries under low-pressure conditions.

This work aims to narrow the knowledge gap and modify the previous thermal-runaway models by considering the effect of ambient pressure on mass loss and energy dissipation. The lumped model is selected to calculate the gas generation and temperature response during the battery thermal runaway. The classical coil heating tests are employed to determine the key parameters for quantifying the energy dissipation during the venting process. Then, the developed model is used to systematically study the influences of ambient pressure, cell heating rate, and venting threshold on battery thermal failure. The temperature-pressure evolution inside batteries before the safety valve opening is compared, and the thermal runaway characteristics under various conditions are discussed. The findings can advance our understanding of battery thermal runaway and offer guidelines for assessing battery thermal safety under low-pressure storage and transportation.

**Table 1**
The recent venting models during battery thermal runaway.

| Cell type | Cathode | Key research topic | Simulation methods | Ref. |
|---|---|---|---|---|
| 18,650 | LCO | Gas generation during venting and thermal runaway | Lumped model | [47, 48] |
| 18,650 | NCM | Effect of free electrolyte and cooling rate on venting and thermal runaway | Lumped model | [49] |
| 18,650 | NCM | Internal pressure and temperature before venting | Lumped model | [50] |
| 18,650 | NCA | Thermal and flow behaviours during venting and thermal runaway | Lumped model & CFD | [51] |
| 18,650 | NCM | Jet flow during venting and flaming during thermal runaway | Lumped model & CFD | [52] |
| 18,650 | NCM | The jet of solid particles and its effect on thermal runaway propagation | Lumped model & CFD | [53] |
| 18,650 | NCM | Spatial distribution of vented gases and air mixing | Lumped model & CFD | [25] |
| prismatic | LFP | Ejected particles from thermal runaway | Lumped model & CFD | [33] |
| 18,650 | NCM | Gas jet behaviours during venting | CFD | [54] |
| 21,700 | NCA | Venting and the temperature distribution of venting fluid | Lumped model & CFD | [55] |

## 2. Model development

### 2.1. Experiment benchmark

The baseline experiments under a low-pressure environment can capture the entire process of battery heating, venting, and thermal runaway, which supports the development of a numerical model. This work considers the coil-heating test for typical 18,650-type cells under various ambient pressures. Fig. 3a shows the developed low-pressure chamber for controlling the environment for battery thermal runaway

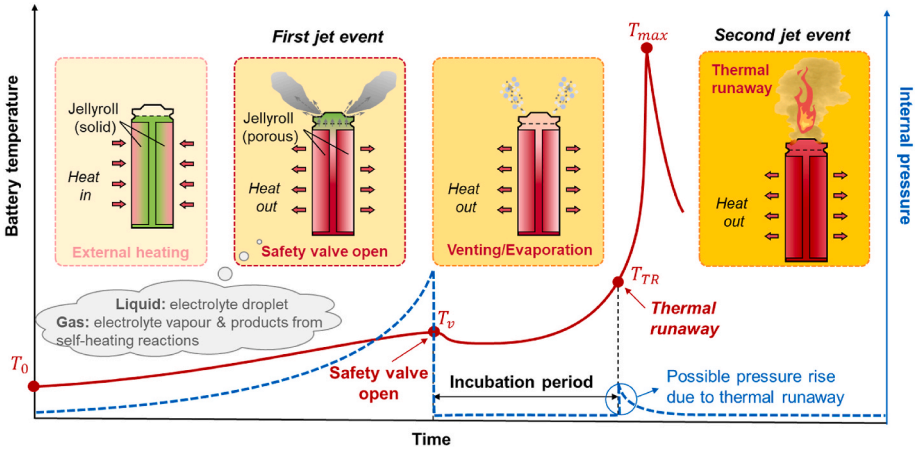


**Fig. 2.** Temperature and internal pressure response for a battery cell exposed to thermal abuse conditions.

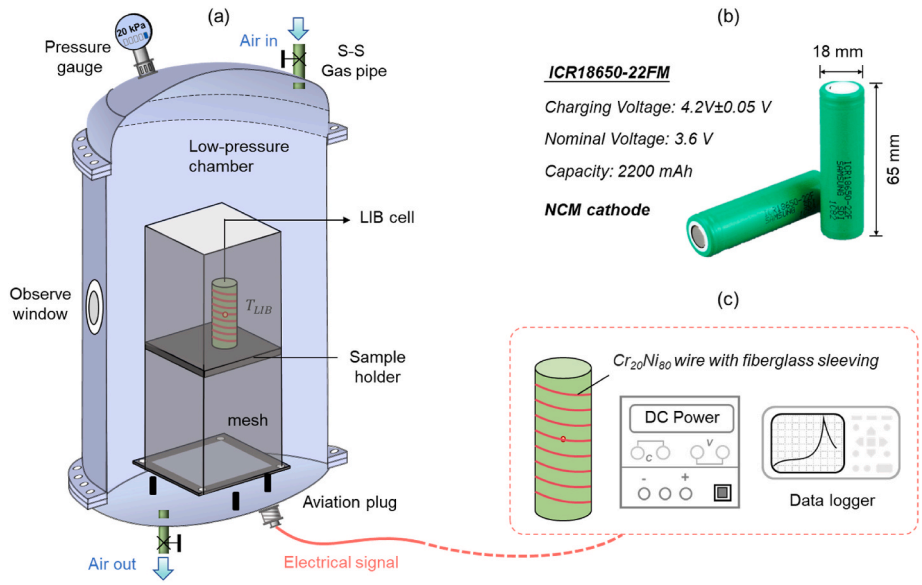


**Fig. 3.** (a) Schematic diagram of the experimental low-pressure chamber, (b) 18,650-type cell, and (c) heating and data collecting methods.

[37]. The chamber walls are constructed from 10-mm thick stainless steel and coated with heat-insulating paint. A fireproof observation window is installed to allow monitoring during tests. The chamber has a volume of 260 L, which is sufficiently large to avoid the gases generated by thermal runaway affecting the ambient pressure. This chamber can maintain a constant pressure ranging from 0.1 kPa to 100 kPa through precisely regulating the air inlet and outlet. Aviation connectors are employed to transmit electrical signals to ensure the airtightness of the low-pressure chamber.

Commercial 18,650-type batteries with a nominal voltage of 3.6 V and capacity of 2200 mA h are tested in this work (Fig. 3b). The cell has the cathode of $LiNi_{0.5}Co_{0.2}Mn_{0.3}O_2$ (NCM523) and the anode of graphite. The electrolyte consists of $LiPF_6$ dissolved in a solvent composed of ethylene carbonate (EC), ethyl methyl carbonate (EMC), and dimethyl carbonate (DMC). The cells from the same patch with an initial mass of around 41 g are selected and fully charged before the tests. The major thermophysical parameters for the battery cell can be found in Ref. [56]. Inside the low-pressure chamber, a sample holder is centrally located for conducting coil heating experiments. Surrounding the sample holder is the fine metal mesh, which is designed to prevent damage to the chamber structure from battery thermal runaway. The widely used heating coil is used to heat the cylindrical cell uniformly and ensure test repeatability [57]. In terms of the coiling heating setup, the 0.25-mm electric resistance wire ($Cr_{20}Ni_{80}$) is enveloped by a high-temperature fibreglass sleeving with a 1-mm diameter and tightly convolved around the cell (Fig. 3c). The DC power supply is used to maintain the heating power constant during the tests. The K-type thermocouple, with an accuracy of ±1 °C, is fixed on the centre surface of the cell and connected to a data logger through an aviation plug for temperature collection. The experimental data are used to determine the critical parameters for the proposed numerical model.

### 2.2. Model description

This work aims to develop a numerical model to reproduce the coil heating tests and analyse the battery thermal runaway under low ambient pressures. Since this study only requires a rapid determination of battery temperature evolution, we selected the lumped model, a computationally efficient approach that is extensively employed in the literature. This method can also be extrapolated to study the complex influences of venting and flaming combustion on battery thermal runaway propagation using CFD modelling [58]. Another reason for using the lumped model is the relatively small size of cylindrical cells (particularly the 18,650-type cells), where temperature gradients are typically neglected for heat generation calculation in the previous works [47–50]. The heat and mass transfer processes during the battery thermal runaway are described by a set of ordinary differential equations (ODEs). As presented in Fig. 4a, three sub-models, including internal reactions, gas generation, and venting, are considered. The internal reaction model is coupled with the gas generation and venting model to calculate the rate of internal reactions, heat generation, and cell temperature variation. Based on the reaction rate and cell temperature, the amount of gases inside the cell can be determined through the gas generation model. The internal pressure is identified according to the gases and the volume of headspace inside the cell using the ideal gas law [25]. Once the difference between internal pressure and ambient pressure exceeds the threshold of the safety valve, the venting model is activated to consider the effect of ambient pressure on reactant loss. The venting model will further update the initial conditions of the internal-reaction model in the following iteration process until the modelling finishes. In other words, the ambient pressure is set as a boundary condition that changes the venting threshold and environmental cooling.

Fig. 4b provides a more detailed explanation of the entire model calculation process. After setting the initial temperature value for the simulation, the ODE solver calculates the instantaneous reaction rates and heat generation rates within the cell based on the conservation equations of energy and mass. These reaction rates and heat generation rates further determine the quantities of reactants and the cell temperature, which facilitates the calculation of the gas generation amount and the corresponding internal pressure. The model can use these parameters to identify critical events during the coil heating process, such as the safety valve opening and thermal runaway, thereby adjusting the initial parameters for the next iteration. The simulation finishes when the solving time ($t$) reaches the predetermined end time ($t_{end}$). The details of ODEs for the conservation of energy and mass will be introduced in later sections. To capture the essential behaviours and improve computational efficiency, the complex thermal runaway process is simplified with the following assumptions. Firstly, the internal temperature and pressure gradients are ignored, and the temperature of gases inside the cell equals the battery average temperature. Additionally, the influence of flaming combustion on the battery surface temperature is ignored since most combustion energy dissipates into the environment.

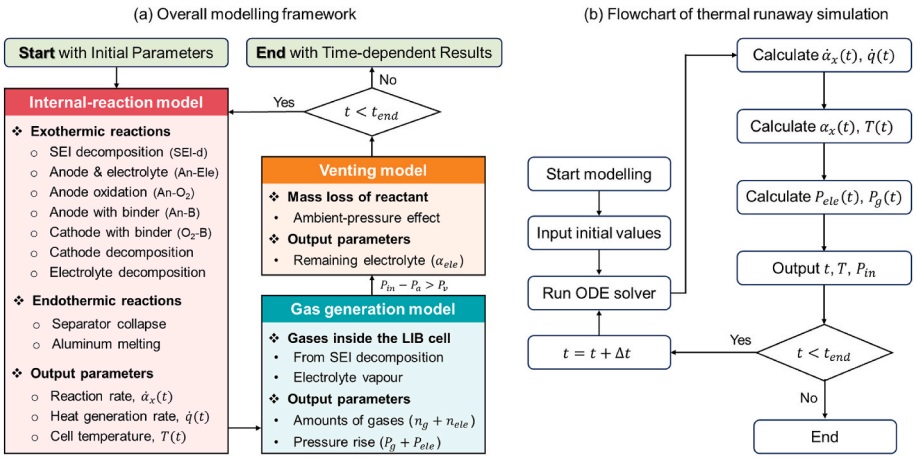


**Fig. 4.** (a) Overall modelling framework and (b) the calculation process for thermal runaway simulation.

### 2.3. Kinetics for internal reactions

The widely adopted reaction mechanisms for batteries exposed to external heating are used in this work. At the beginning of the self-heating reaction, the reaction rate for SEI decomposition (SEI-d) can be expressed as

$$\dot{\alpha}_{\text{SEI-d}} = \frac{d\alpha_{\text{SEI-d}}}{dt} = Z_{\text{SEI-d}}(\alpha_{\text{SEI-d}})^{5.5} \exp\left(-\frac{E_{\text{a,SEI-d}}}{RT}\right) \tag{1}$$

where $\alpha_{\text{SEI-d}}$ is the non-dimensional amount for the reactant in the SEI layer, $Z_{\text{SEI-d}}$ is a pre-exponential factor, $E_{\text{a,SEI-d}}$ is the activation energy, $R$ is the universal gas constant, and $T$ is the cell temperature, respectively. Note that the SEI-d rection order in this work is 5.5, agreeing with the parameters in previous studies [49,50]. Upon loss of SEI protection, intercalated lithium in the anode reacts with organic solvents in the electrolyte (An-Ele), which is also referred to as the SEI regeneration reaction. The rate of this An-Ele reaction is given by

$$\dot{\alpha}_{\text{An-Ele}} = \frac{d\alpha_{\text{An-Ele}}}{dt} = Z_{\text{An-Ele}}\alpha_{\text{An-Ele}}\, exp\left(-\frac{z}{z_0}\right) exp\left(-\frac{E_{\text{a,An-Ele}}}{RT}\right) \tag{2}$$

where $z$ stands for the non-dimensional thickness of the SEI layer, which increases with the reaction rate. The initial thickness ($z_0$) is set as 0.033 [59]. As reviewed in the introduction, the An-Ele reaction significantly contributes to heat generation, thus potentially initiating thermal runaway [20]. Meanwhile, redox reactions between electrodes would be triggered [60]. The oxygen released from the cathode will oxidise the anode (An-$O_2$), and the reaction rate for An-$O_2$ is

$$\dot{\alpha}_{\text{An-O}_2} = \frac{d\alpha_{\text{An-O}_2}}{dt} = Z_{\text{An-O}_2}\alpha_{\text{An-O}_2}\, exp\left(-\frac{E_{\text{a,An-O}_2}}{RT}\right) \tag{3}$$

where $\alpha_{\text{An-O}_2}$ is the non-dimensional amount for the reactant. As this reaction is coupled with the An-Ele, the coupled consumption of reactant mass will be considered and delivered in Section 2.5. The binder-related reactions include anode-binder (An-B) and the oxygen released from the cathode with the binder ($O_2$-B). The reaction rates are listed below.

$$\dot{\alpha}_{\text{An-B}} = \frac{d\alpha_{\text{An-B}}}{dt} = Z_{\text{An-B}}\alpha_{\text{An-B}}\, exp\left(-\frac{E_{\text{a,An-B}}}{RT}\right) \tag{4}$$

$$\dot{\alpha}_{\text{O}_2\text{-B}} = \frac{d\alpha_{\text{O}_2\text{-B}}}{dt} = Z_{\text{O}_2\text{-B}}(\alpha_{\text{O}_2\text{-B}})^2\, exp\left(-\frac{E_{\text{a, O}_2\text{-B}}}{RT}\right) \tag{5}$$

Then, the reaction rate for cathode decomposition (Cat) is

$$\dot{\alpha}_{\text{Cat}} = \frac{d\alpha_{\text{Cat}}}{dt} = Z_{\text{Cat}}(\alpha_{\text{Cat}})^{1.5}\, exp\left(-\frac{E_{\text{a,Cat}}}{RT}\right) \tag{6}$$

Following the lumped thermal runaway model in previous works [49,50], the reaction order for cathode decomposition is set as 1.5. Finally, the electrolyte decomposition (Ele) is recognised as an auto-catalytic reaction, with a reaction rate of

$$\dot{\alpha}_{\text{Ele}} = \frac{d\alpha_{\text{Ele}}}{dt} = Z_{\text{Ele}}\alpha_{\text{Ele}}(1-\alpha_{\text{Ele}})exp\left(-\frac{E_{\text{a,Ele}}}{RT}\right) \tag{7}$$

The parameters for calculating the rate of exothermic reactions are listed in Table 2.

It should be noted that most parameters are derived from Refs. [49, 50], while the parameters related to the An-$O_2$ reaction are fitted by experimental data. This adjustment is reasonable because the reactions associated with the cathode have a negligible impact on the onset of thermal runaway but primarily influence the maximum temperature after thermal runaway. Generally, in NCM cells, the higher the nickel content, the stronger the intensity of this reaction. Since the nickel content and capacity of the cells used in our study differ from those reported in the referenced literature, we primarily adjusted the reaction enthalpy of this reaction to align the simulation results with the maximum temperature in experimental data. Meanwhile, the adjustments made to the activation energy and the pre-exponential factor were minor, with their values remaining close to those reported in the literature [49,50]. These details have been clarified in the revised manuscript, and we hope this explanation can address your concerns.

### 2.4. Energy conservation

For the battery cell under external coil heating, the energy conser-

**Table 2**
Parameters for calculating the exothermic reaction rate.

| Description of reaction $x$ | $Z_x$ ($s^{-1}$) | $E_{a,x}$ ($J{\cdot}mol^{-1}$) | $\Delta H_x$ ($J{\cdot}g^{-1}$) | Equation (#) |
|---|---|---|---|---|
| SEI-d | $5.32 \times 10^{10}$ [50] | $9.6 \times 10^4$ [50] | 257.0 [50] | (1) & (9) |
| An-Ele | $2.51 \times 10^{13}$ [49] | $1.3238 \times 10^5$ [49] | 1714.0 [49] | (2) & (9) |
| An-$O_2$ | $2.6681 \times 10^{13}$ [–] | $1.4661 \times 10^5$ [–] | 2242.4 [-] | (3) & (9) |
| An-B | $4.9679 \times 10^{15}$ [50] | $1.9549 \times 10^5$ [50] | 108.5 [50] | (4) & (9) |
| $O_2$-B | $6.5429 \times 10^{13}$ [50] | $1.7785 \times 10^5$ [50] | 452.1 [50] | (5) & (9) |
| Cat | $5.3481 \times 10^5$ [50] | $1.0934 \times 10^5$ [50] | 434.0 [50] | (6) & (9) |
| Ele | $4.7320 \times 10^7$ [50] | $8.9490 \times 10^4$ [50] | 1300 [50] | (7) & (9) |

vation equation follows

$$m_{\mathrm{LIB}} c_{\mathrm{LIB}} \frac{dT}{dt} = \dot{q}_{\mathrm{ex}} + \sum \dot{q}_{\mathrm{x}} + \dot{q}_{\mathrm{diss}} + \dot{q}_{\mathrm{evap}} + \sum \dot{q}_{\mathrm{i,melt}} + \dot{m}_{\mathrm{v}} \Delta H_{\mathrm{v}} \quad (8)$$

where $m_{\mathrm{LIB}}$ is the mass of the battery cell, $c_{\mathrm{LIB}} = 1100\ \mathrm{J\ kg^{-1}\ K^{-1}}$ is the specific heat of the cell, $\dot{q}_{\mathrm{ex}}$ is the effective heating rate, $\sum \dot{q}_{\mathrm{x}}$ is the overall heat generation rate of exothermic reactions, $\dot{q}_{\mathrm{diss}}$ is the heat dissipation to the environment, $\dot{q}_{\mathrm{evap}}$ is the heat absorption due to electrolyte evaporation, $\sum \dot{q}_{\mathrm{i,melt}}$ is induced by the melting process of the separator and aluminium current collector, and $\dot{m}_{\mathrm{v}} \Delta H_{\mathrm{v}}$ is the energy loss during the venting process, respectively. It should be noted that the joule heating caused by ISC is not considered here, as it contributes negligibly to the thermal runaway of NCM cells [20]. The methods for determine the effective heating rate have been introduced by our previous work [61]. According to the literature, the released materials include the gases generated from SEI-d reactions and the electrolyte evaporation. The mass loss rate $\dot{m}_{\mathrm{v}}$ is determined by mass conservation equations in the next section, and the value of specific entropy ($\Delta H_{\mathrm{v}}$) is selected from the database provided by the National Institute of Standards and Technology (NIST) [62].

For the heat source term of $\sum \dot{q}_x$, it can be written as

$$\sum \dot{q}_{\mathrm{x}} = \sum m_{\mathrm{x}} \Delta H_{\mathrm{x}} \dot{\alpha}_{\mathrm{x}} \quad (9)$$

where $m_{\mathrm{x}}$ is the mass of the reactant $x$, $\Delta H_{\mathrm{x}}$ is the corresponding heat of reaction, and $\dot{\alpha}_{\mathrm{x}}$ is the reaction rate. The environmental cooling rate $\dot{q}_{\mathrm{diss}}$ is given by

$$\dot{q}_{\mathrm{diss}} = -h_{\mathrm{c}} A (T - T_{\mathrm{a}}) \quad (10)$$

where $h_{\mathrm{c}}$ is the effective cooling coefficient that fitted by the tests under various ambient pressures [36], $A$ is the cell surface area, and $T_{\mathrm{a}}$ is the ambient temperature. The heat absorption rate during the electrolyte evaporation, $\dot{q}_{\mathrm{evap}}$, can be expressed as

$$\dot{q}_{\mathrm{ele,vap}} = -\frac{dm_{\mathrm{ele,vap}}}{dt} \Delta H_{\mathrm{ele,evap}} \quad (11)$$

where $\Delta H_{\mathrm{evap}}$ is the heat of evaporation. Regarding the melting process of the separator and aluminium collector, the solid-liquid phase change is illustrated using a sigmoid function [49]. Then, the heat absorption rate during the melting process ($\dot{q}_{\mathrm{i,melt}}$) is

$$\dot{q}_{\mathrm{i,melt}} = -\frac{d(\varphi_{\mathrm{i,melt}} m_{\mathrm{i}})}{dt} \Delta H_{\mathrm{i,melt}} \quad (12)$$

where $\Delta H_{\mathrm{i,melt}}$ is the fusion heat, $\varphi_{\mathrm{i,melt}}$ is the liquid fraction during the solid-liquid phase change process and can be written as

$$\varphi_{i,melt} = \frac{1}{1 + \exp\left[(T_{\mathrm{i,melt}} - T) \cdot b_{\mathrm{i,melt}}\right]} \quad (13)$$

where $b_{\mathrm{i,melt}}$ is a non-dimensional parameter for the correlation between liquid fraction and temperature. The parameters for calculating the $\dot{q}_{\mathrm{evap}}$ and $\dot{q}_{\mathrm{i,melt}}$ are summarised in Table 3.

### 2.5. Mass conservation

The mass conservation equation serves as a crucial link between the internal reaction and gas generation models (Fig. 4a), primarily used to calculate the depletion of reactants and the generation of gases. For the SEI-d reaction, the mass conservation equation is

$$\alpha_{\mathrm{SEI\text{-}d}} = \alpha_{\mathrm{SEI\text{-}d,0}} - \int \dot{\alpha}_{\mathrm{SEI\text{-}d}} dt \quad (14)$$

where the $\alpha_{SEI-d,0}$ is the initial value of dimensionless concertation for the SEI layer. As the An-$O_2$ reaction is coupled with the An-Ele reaction,

**Table 3**
Parameters for describing the evaporation and melting heat [50,63].

| Process | Parameter | Symbol | Unit | Value | Equation (#) |
|---|---|---|---|---|---|
| Evaporation | Evaporation heat | $\Delta H_{\mathrm{ele,vap}}$ | $\mathrm{J{\cdot}g^{-1}}$ | 520 | (11) |
| Separator collapse | Onset temperature | $T_{\mathrm{sp,melt}}$ | °C | 171.4 | – |
| | Fusion heat | $\Delta H_{\mathrm{sp,melt}}$ | $\mathrm{J{\cdot}g^{-1}}$ | 150 | (12) |
| | Dimensionless coefficient | $b_{\mathrm{sp,melt}}$ | – | 0.25 | (13) |
| Aluminium melting | Onset temperature | $T_{\mathrm{Al,melt}}$ | °C | 660.46 | – |
| | Fusion heat | $\Delta H_{\mathrm{Al,melt}}$ | $\mathrm{J{\cdot}g^{-1}}$ | 389 | (12) |
| | Dimensionless coefficient | $b_{\mathrm{Al,melt}}$ | – | 0.055 | (13) |

the mass conservation for the active material in the anode should be [60]

$$\alpha_{\mathrm{An}} = \alpha_{\mathrm{An,0}} - \int \dot{\alpha}_{\mathrm{An-Ele}} dt - \int \dot{\alpha}_{\mathrm{An\text{-}O_2}} dt \quad (15)$$

For other exothermic reactions, the mass conservation equation can be expressed as

$$\alpha_{\mathrm{An\text{-}B}} = \alpha_{\mathrm{An\text{-}B,0}} - \int \dot{\alpha}_{\mathrm{An\text{-}B}} dt \quad (16)$$

$$\alpha_{\mathrm{O_2\text{-}B}} = \alpha_{\mathrm{O_2\text{-}B,0}} - \int \dot{\alpha}_{\mathrm{O_2\text{-}B}} dt \quad (17)$$

$$\alpha_{\mathrm{Cat}} = \alpha_{\mathrm{Cat,0}} - \int \dot{\alpha}_{\mathrm{Cat}} dt \quad (18)$$

$$\alpha_{\mathrm{Ele}} = \alpha_{\mathrm{Ele,0}} - \int \dot{\alpha}_{\mathrm{Ele}} dt \ (t \le t_{\mathrm{v}}) \quad (19)$$

The values for the above mass conservation equation are listed in Table 4.

The above reactions raise the cell temperature and generate a substantial amount of gas to increase the internal pressure. Before the safety valve opens, the primary gases inside the cell are produced from SEI decomposition and electrolyte vapour. Although the organic solvents in the electrolyte include EC, EMC, and DMC, numerous theoretical and experimental studies have shown that DMC vapour significantly contributes to activating the safety valve [23]. Therefore, we assume that the electrolyte vapour is primarily composed of DMC and treat it as the ideal gas to simplify the complex vaporisation process. For gases generated from SEI-d reaction, the mass conservation is

$$\alpha_{\mathrm{gas\text{-}SEI}} = \alpha_{\mathrm{SEI\text{-}d,0}} - \alpha_{\mathrm{SEI\text{-}d}} \quad (20)$$

$$m_{\mathrm{gas\text{-}SEI}} = m_{\mathrm{gas\text{-}SEI,0}} \cdot \alpha_{\mathrm{gas\text{-}SEI}} \quad (21)$$

**Table 4**
The mass-related values for the exothermic reactions [50].

| Reaction | Reactant mass (g) | Initial dimensionless concertation | Value (–) | Equation (#) |
|---|---|---|---|---|
| SEI decomposition | 9.92 | $\alpha_{\mathrm{SEI\text{-}d,0}}$ | 0.15 | (14) |
| Anode with electrolyte | 9.92 | $\alpha_{\mathrm{An\text{-}Ele,0}}$ | 0.52 | (15) |
| Anode oxidation | 9.92 | $\alpha_{\mathrm{An\text{-}O_2,0}}$ | 1 | (15) |
| Anode with binder | 9.92 | $\alpha_{\mathrm{An\text{-}B,0}}$ | 1 | (16) |
| Oxygen from the cathode with binder | 14.00 | $\alpha_{\mathrm{O_2\text{-}B,0}}$ | 1 | (17) |
| Cathode decomposition | 14.00 | $\alpha_{\mathrm{Cat,0}}$ | 1 | (18) |
| Electrolyte decomposition | 4.4 | $\alpha_{\mathrm{Ele,0}}$ | 0.26 | (19) |

where the $m_{\text{gas-SEI},0} = 0.026$ g is the entire mass of gases released from the SEI-d reaction [50]. According to the chemical reaction of SEI decomposition, the SEI-d reaction will generate $C_2H_4$, $CO_2$, and $O_2$. As the mole ration of these gas products is around 1:1:0.5, the relative molecular mass of the gas mixture ($M_g$) is about 35.2 g· mol$^{-1}$ [64]. Then, the amount of gas ($n_g$) is

$$n_g = \frac{m_{\text{gas-SEI}}}{M_g} \tag{22}$$

The internal pressure caused by SEI-generated gas is given by

$$P_g = \frac{n_g RT}{V_{\text{space}}} \tag{23}$$

In terms of the internal pressure increase contributed by electrolyte evaporation ($P_{\text{ele}}$), it follows the Antoine's equation as [52]

$$P_{\text{ele}} = \exp\left(a - \frac{b}{T(K) + c}\right) \tag{24}$$

Thus, the total internal pressure ($P_{\text{in}}$) can be calculated by

$$P_{\text{in}} = P_g + P_{\text{ele}} + P_0 \tag{25}$$

where $P_0 = 101$ kPa is the initial pressure inside the cell. The amount of electrolyte vapour can be determined by

$$n_{\text{ele,vap}} = \frac{P_{\text{ele}} V_{\text{space}}}{RT} \tag{26}$$

Then, the mass of the evaporated electrolyte is

$$m_{\text{ele,vap}} = n_{\text{ele,vap}} M_{\text{ele}} \tag{27}$$

Once the value of $P_{\text{in}} - P_a$ exceeds the threshold of the safety valve ($P_v$), the safety venting will occur. At this moment, the internal gases and electrolyte droplets will jet from the inner cell. After the safety valve opens, the cell enters the venting mode, i.e., the incubation period. Previous studies have studied and modelled the electrolyte loss during this period (i.e., venting-to-thermal-runaway). For example, the model developed by Ostanek et al. [49] proposed a theoretical loss rate for electrolyte. They assumed that when the liquid fraction was high, the electrolyte loss would exhibit a high rate. Once the free electrolyte was depleted, the loss rate of the electrolyte slowed down. Such a process was also observed by Huang et al. [55] in their experiments. Specifically, after the safety valve opens, the cell mass undergoes two stages during the venting process.

In the first stage, electrolyte droplets are rapidly released in a short time, and in the second stage, the electrolyte vapour and internal gases diffuse at a slower rate. The first stage lasts less than 5 s, with a loss rate more than 200 times that of the subsequent slow evaporation. Moreover, the significant liquid phase during the venting process can be found through the Schlieren technology [32]. Our previous experiments under low pressure also observed this process [36], where the loss of electrolytes in the first stage is more severe under low ambient pressure. Since the reaction intensity of An-Ele significantly decreases as the electrolyte mass reduces, the heat accumulation in the battery during the venting stage slows down under low ambient pressure. The literature also indicates that the rapid release duration for electrolytes in the first stage is uncertain [55], and the reaction heat for An-Ele decreases with the reduction of electrolyte mass [65]. Considering the complexity of this process, this model simplifies the first stage to an instantaneous loss of a percentage of the electrolyte mass. Thus, the loss rate of electrolyte droplets during the venting process in Eq. (19) can be modified as

$$\alpha_{\text{Ele}} = (1-\eta)\alpha_{\text{Ele,v}} - \int \dot{\alpha}_{\text{Ele}} dt \quad (t > t_v) \tag{28}$$

where $\alpha_{\text{Ele,v}}$ represent the non-dimensional concentration of the electrolyte at the onset moment of venting, and the $\eta$ represents the effective electrolyte reactant loss that engaged in thermal runaway reactions. This decrease in electrolyte consumption can highlight the effect of ambient pressure on mass loss and energy dissipation during the venting process. Theoretically, the value of $\eta$ increases with the reduced ambient pressure, which will be fitted through the experiments at various low-pressure conditions. All key parameters for evaluating the progress of gas generation and venting are explained in Table 5.

## 3. Results and discussions

### 3.1. Thermal runaway characteristics

This section employs coil heating tests at 60 kPa to exhibit the thermal runaway characteristics and the determination process of $\eta$. The cell surface temperature data from the experiment are depicted in Fig. 5a. The classical three distinct stages are demonstrated by temperature curve as heating, venting, and thermal runaway. The cell temperature gradually increases during the heating phase. A slight decrease in temperature is observed at approximately 385 s due to the activation of the safety vent. After venting for a while, there is a rapid temperature increase, indicating the onset of thermal runaway. The simulation results show excellent agreement with the experimental data, where the mass loss ratio ($\eta$) is fitted as 0.35. The numerical model especially successfully captures the above key events during cell thermal failure. The evolution of internal pressure ($P_{in}$) also shows a similar trend to that of the literature [55]. As the safety valve threshold in this work is 2.2 MPa, the safety venting occurs when the value of $P_{in}$ reaches 2.26 MPa. In short, the strong matching between experimental and numerical data suggests the rationality of the model assumptions and the reliability of the model results. Therefore, this model can be used to predict the thermal behaviours of the cell under external heating tests.

Fig. 5b demonstrates the temperature rise rate and internal pressure varying with the cell temperature for the simulated case. Under the external coil heating, the temperature rise rate maintains around 0.3 °C s$^{-1}$ when the cell temperature is lower than 80 °C. Then, the temperature rise rate gradually increases due to the occurrence of internal self-heating reactions. The curve of the temperature rise rate in Fig. 5b can help us to identify the characteristic temperatures during the thermal runaway. Specifically, the safety venting temperature ($T_v$) is defined as the temperature at the moment that the self-heating rate becomes negative. The onset temperature for the thermal runaway ($T_{TR}$) refers to the point at which a temperature rise rate exceeds the 10 °C s$^{-1}$. Such a definition is relatively conservative and is based on the observation of experimental phenomena and methods reported in the literature [66]. The value of $T_{max}$ corresponds to the maximum surface temperature after thermal runaway, which depends on the cell capacity, cathode chemistry, and environmental cooling condition.

The partial pressure of gas generated by SEI-d reaction ($P_g$), electrolyte vapour ($P_{ele}$), and the total internal pressure ($P_{in}$) are depicted in Fig. 5b. Since the cell safety valve opens to release pressure when the internal pressure reaches 2.2 MPa, this work only records the evolution of internal pressure before the safety venting. It is apparent that the rise

**Table 5**
The parameters for describing the gas generation and venting process [50].

| Parameter description | Symbol | Unit | Value | Equation (#) |
|---|---|---|---|---|
| Molecular mass for SEI-d gas | $M_g$ | g·mol$^{-1}$ | 35.2 | (22) |
| Void space volume inside the cell | $V_{\text{space}}$ | m$^3$ | $1.157 \times 10^{-6}$ | (23) |
| Antoine's equation for electrolyte evaporation | $a$ | – | 18.55 | (24) |
| Antoine's equation for electrolyte evaporation | $b$ | $K$ | 8661.4 | (24) |
| Antoine's equation for electrolyte evaporation | $c$ | $K$ | 270.16 | (24) |

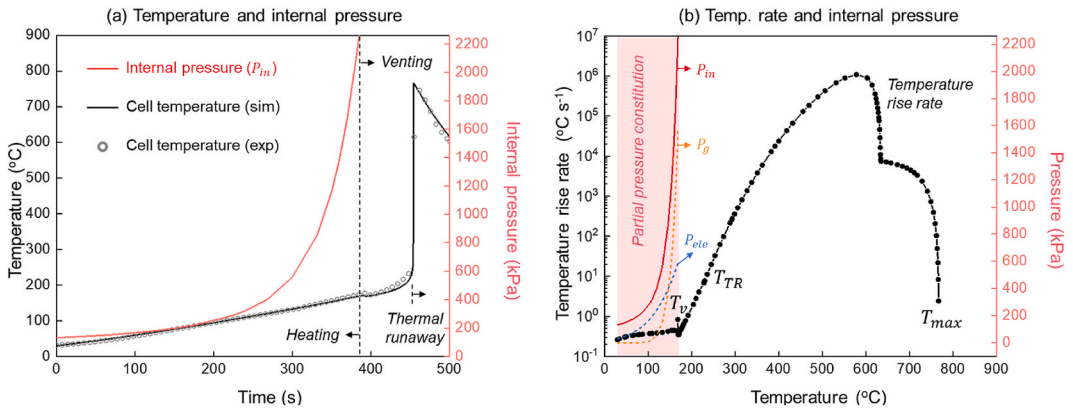


**Fig. 5.** (a) The comparison of experimental and numerical results for cells at 60 kPa and (b) the simulated temperature rise rate and internal pressure varying with cell temperature.

in internal pressure is primarily driven by electrolyte evaporation when the cell temperature is low. After the initiation of the SEI-d reaction, the partial pressure of the generated gas ($P_g$) exponentially increases and finally exceeds the value of $P_{ele}$. When the safety valve opens, the partial pressure of the gas produced by the SEI-d reaction is 1.568 MPa, accounting for approximately 69.4 % of the internal pressure. The partial pressure constitution observed in this study is also consistent with experimental findings in the literature [31]. Therefore, we can conclude that the venting gases of this cell are mainly from the SEI-d reactions.

### 3.2. Effect of ambient pressure

In this work, three ambient pressures of 100 kPa, 60 kPa, and 20 kPa are selected to illustrate the effect of ambient pressure on thermal runaway. 100 kPa is regarded as the standard atmospheric pressure. 60 kPa is the typical pressure for high-altitude regions with an elevation of 4000 m [5], while 20 kPa is the ambient pressure encountered during high-altitude cruising in commercial air transport [67]. The semi-empirical model proposed in this work will employ experimental data to determine the effective mass loss ratio ($\eta$) of electrolytes under different ambient pressures.

The fitting results for temperature variation are exhibited in Fig. 6a. The safety venting temperatures for these three conditions are almost similar in the experimental data, agreeing with the experimental findings in previous studies [39]. The thermal runaway time is delayed from 416 s to 479 s as the ambient pressure decreases from 100 kPa to 20 kPa. This is because the cell ejects more electrolyte under low ambient pressure after the safety valve opens, resulting in a slower reaction rate inside the cell during the venting period. Based on the experimental data, the values of $\eta$ at 100 kPa, 60 kPa, and 20 kPa are fitted as 0.07, 0.35, and 0.64, respectively. As expected, the value of $\eta$ decreases with increasing ambient pressure. In other words, incorporating the equivalent mass losses of 7 % and 64 % for electrolytes into the mass conservation equations allows for a good reproduction of the experimental results of thermal runaway tests at 100 kPa and 20 kPa. Thus, the model proposed in this work and the equivalent mass loss parameters can offer new insights into predicting thermal runaway behaviour under low-pressure conditions. It should be noted that there is still some discrepancy in maximum temperature between the simulation results and experimental data at 100 kPa. However, this issue is common in literature due to the inherent uncertainties in thermal runaway experiments [68,69]. The simulation results are acceptable, considering that the error for both the onset time and thermal runaway onset temperature at 100 kPa is less than 10 %.

Fig. 6b further compares the temperature rise rate for cells under various ambient conditions. Similarly, the temperature rise rate of cells progressively escalates due to continuous external heating and the triggered self-heating reactions. Cells at different ambient pressures exhibit similar temperatures for safety venting ($T_v$). However, after safety venting, the effect of ambient pressure on mass loss and energy dissipation becomes apparent in the temperature rise rate. With a higher mass loss fraction observed in cells under low ambient pressure, the temperature rise rate of cells at 20 kPa decreases to nearly 0.25 °C s$^{-1}$, representing its lowest value. Nonetheless, the internal reactions continue to generate heat, causing the temperature rise rate of cells to rebound quickly. When the temperature reaches around 230 °C, the

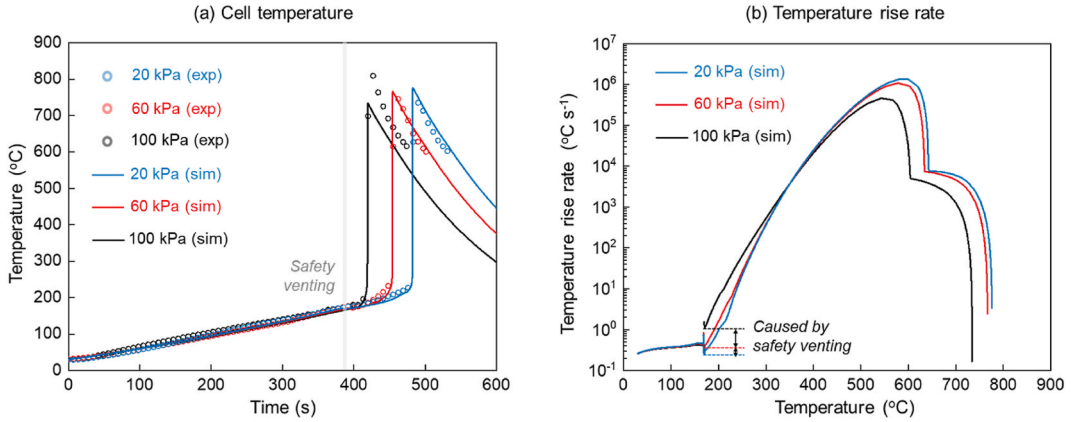


**Fig. 6.** (a) Experimental and numerical data at various ambient pressures, as well as (b) simulation data for the temperature rise rate and internal pressure varying with cell temperature.

temperature rise rate of the cell at 20 kPa exceeds 10 °C $s^{-1}$, confirming the onset of thermal runaway. In short, this semi-empirical model can be used to analyse the other influencing factors for thermal runaway under sub-atmospheric pressures.

### 3.3. Effect of cell heating rate

In international standards related to battery safety, common methods for triggering thermal runaway include nail penetration, overcharge, and external heating. External heating has been proven to be the most reproducible testing method [70], but the selection of heating power varies among different standards. For example, the Chinese standard GB 38031 specifies the range of maximum heater power based on the cell energy capacity. For a battery with an energy capacity lower than 100 W h, the maximum heater power should range from 30 to 300 W. Additionally, the American standard UL 9540 A requires the initial surface heating rate of the battery to be between 4 and 7 °C $min^{-1}$. To better highlight the impact of heating power on thermal runaway under different ambient pressures, this study follows the UL 9540 A requirements. It sets a constant temperature rise rate for the cell. Then, the energy conservation equation for the cell in Eq. (8) should be rewritten as

$$m_{\mathrm{LIB}} c_{\mathrm{LIB}} \frac{dT}{dt} = \dot{q}_{\mathrm{ex},0} + \sum \dot{q}_{\mathrm{x}} + \dot{q}_{\mathrm{evap}} + \sum \dot{q}_{\mathrm{i,melt}} + \dot{m}_{\mathrm{v}} \Delta H_{\mathrm{v}} \tag{29}$$

where $\dot{q}_{\mathrm{ex},0} = m_{\mathrm{LIB},0} c_{\mathrm{LIB}} \dot{T}_{\mathrm{e}}$ is the effective external heating rate, and $\dot{T}_e$ is the constant temperature rise rate. The effective heating rates of 4, 7, 10, and 30 °C $min^{-1}$ are selected in this work.

Taking the cell at 60 kPa as an example, the temperature evolution curves under different heating rates are depicted in Fig. 7a. As expected, the onset time for thermal runaway ($t_{\mathrm{TR}}$) decreases as the heating rate increases. Specifically, the value of $t_{\mathrm{TR}}$ decreases from 2204 s–338 s as the heating rate increases from 4 °C $min^{-1}$ to 30 °C $min^{-1}$. This is because the high heating rate can accelerate internal chemical reactions that generate additional heat, resulting in a faster onset of thermal runaway [57]. Additionally, the temperature for safety venting ($T_{\mathrm{v}}$) slightly increases with the cell heating rate. As the heating rate increases from 4 °C $min^{-1}$ to 30 °C $min^{-1}$, the value of $T_v$ rises from 144 °C to 172 °C, with an increment of about 19.5 %. Due to the similar $T_{\mathrm{v}}$ at different ambient pressures, this positive correlation is presented in Fig. 7b. The reason for such an upward trend is that, at a higher heating rate, the cell temperature rises quickly, leading to a relatively short duration for the SEI-d reaction. Consequently, the proportion of decomposition gases inside the cell is lower. The battery requires more time to accumulate gases internally, resulting in a higher temperature when safety venting occurs.

The partial pressure ratio ($\delta$) is defined to elucidate the impact of SEI-d gas on the increase in internal pressure. It is given by

$$\delta = \frac{P_{\mathrm{g}}}{P_{\mathrm{g}} + P_{\mathrm{ele}}} \times 100\% \tag{30}$$

A high value of $\delta$ indicates that the gas produced by the SEI-d reaction significantly contributes to the opening of the safety valve. The coupling effects of ambient pressure and external heating rate on such a ratio are exhibited in Table 6. Before the safety venting, the battery remains closed, so the influence of ambient pressure on this ratio can be neglected. As the heating power increases, this ratio decreases, indicating that the vaporised electrolyte increasingly contributes to the opening of the safety valve. Since the vaporised electrolyte is theoretically only related to the battery temperature, the higher the heating power, the higher the temperature ($T_{\mathrm{v}}$) at which the safety valve opens (Fig. 7b).

After the safety venting, the time intervals between safety venting and thermal runaway ($\Delta t$) under the various ambient pressures and heating rates are depicted in Fig. 7b. Apparently, the value of $\Delta t$ decreases with the heating rate, indicating a shorter incubation period under a faster heating condition. For cells at 100 kPa, the value of $\Delta t$ reduces from around 145 s–12 s as the heating rate increases from 4 °C $min^{-1}$ to 30 °C $min^{-1}$. As this venting period could serve as a warning for thermal runaway or allow for the implementation of mitigation strategies [71], extreme overheating leaves the battery protection system with insufficient time to respond and prevent the occurrence of thermal runaway. In other words, if the battery cell experiences thermal failure at a slower rate, the incubation period will be extended, providing the protection system with more time to initiate emergency responses. Furthermore, the extension of venting time due to lower heating rates is particularly pronounced under low ambient pressure conditions. Decreasing the heating rate from 10 °C $min^{-1}$ to 4 °C $min^{-1}$ results in a 102 % prolongation of venting time for batteries at 100 kPa; while at 20 kPa, the extension is even more substantial at 286 %. Therefore, when the cell experiences thermal failure at a slower rate under low ambient pressure, implementing measures such as immersion cooling [72] or forced ventilation during the venting period can significantly enhance the probability of preventing thermal runaway.

**Table 6**
The value of $\delta$ varies with ambient pressure and external heating rate.

| | 4 °C $min^{-1}$ | 7 °C $min^{-1}$ | 10 °C $min^{-1}$ | 30 °C $min^{-1}$ |
|---|---|---|---|---|
| 20 kPa | 82.1 % | 79.4 % | 77.4 % | 70.7 % |
| 60 kPa | 82.3 % | 79.6 % | 77.7 % | 71.0 % |
| 100 kPa | 82.5 % | 79.9 % | 77.9 % | 71.3 % |

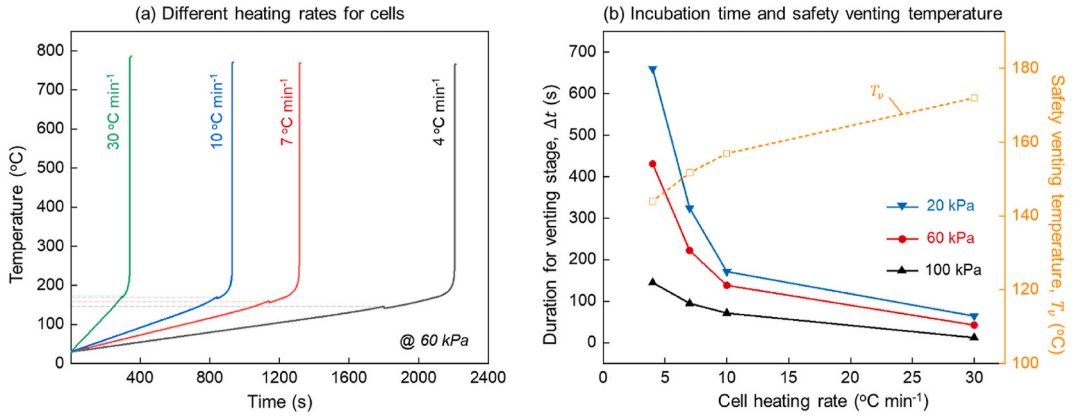


**Fig. 7.** Effect of cell heating rate on (a) temperature evolution at 60 kPa and (b) safety venting temperature, as well as the time interval between safety venting and thermal runaway.

### 3.4. Effect of the safety valve threshold

As mentioned above, lower ambient pressure and heating power can result in an extended venting (or incubation) period, thereby delaying the onset of thermal runaway. Although the impact of ambient pressure on internal gas generation before the safety valve opening can be considered negligible, it remains essential to study the influences of the safety valve threshold on internal gas generation. The threshold of the safety valve determines the pressure at which venting occurs, affecting the timing and content of gas release during a thermal event. Understanding its impact can provide critical information for designing gas detection and warning systems during battery venting, facilitating the implementation of appropriate countermeasures for thermal runaway mitigation under varying ambient pressures.

The effect of the safety valve threshold on thermal runaway characteristics is presented in Fig. 8, with a typical heating rate of 4 °C $min^{-1}$. Six values from 1.2 MPa to 2.2 MPa are employed for $P_v$, the commonly used safety valve thresholds in cylindrical cells [31]. Fig. 8a shows the safety venting time ($t_v$) and temperature ($T_v$) varying with the safety valve pressure ($P_v$). As expected, both the values of $t_v$ and $T_v$ reduce as $P_v$ decreases. When the safety valve threshold is reduced from 2.2 MPa to 1.2 MPa, the activation time of the safety valve ($t_v$) is advanced by approximately 149 s. The battery temperature when the safety valve opens also decreases by about 8 %. At the moment, for safety venting, the partial pressure ratio for SEI-d gases ($\delta$) increases with the safety valve threshold. Specifically, $\delta$ is 73.5 % when $P_v$ is 1.2 MPa. When $P_v$ is 2.2 MPa, $\delta$ increases to 82.3 %. Thus, the gas produced by internal reactions becomes increasingly significant for triggering safety venting as the safety valve threshold increases. Moreover, the time interval between safety venting and thermal runaway (i.e., incubation period, $\Delta t$) exhibits a negative correlation with the safety valve threshold. When the safety valve threshold is lower, the gases generated inside the cell are more easily vented, leading to an earlier safety valve opening and a lower cell temperature. After the safety valve opens early, the cell undergoes a rapid cooling phase followed by a slow temperature rise. Due to the slower heat accumulation during this stage, cells with lower safety valve thresholds have longer incubation periods and delayed thermal runaway trigger times.

### 3.5. Implications and challenges

The proposed model can significantly advance the previous experimental works under low pressure conditions. Building on the above discussions, we have numerically explored the effects of ambient pressure, cell heating rate, and safety valve threshold on venting and thermal runaway. Before the opening of the safety valve (i.e., safety venting), the rise in internal pressure is initially driven by the vaporisation of the electrolyte and gradually becomes dominated by gases produced from internal reactions. A higher safety valve threshold results in a later opening time, making the decomposition gases more significant in the rapid internal pressure increase. Once the safety valve opens, the cell enters the venting mode, referred to as the incubation period of thermal runaway. During this period, lower ambient pressure causes a more significant loss of electrolyte droplets, resulting in a relatively low heat accumulation rate and an extended incubation period for thermal runaway. This prolonged incubation period under low ambient pressure is more pronounced at lower external heating rates. Compared with previous works, this study could provide new insights into strategies for mitigating thermal runaway under low ambient pressure conditions. On the one hand, the proposed model can predict the timing of safety venting and thermal runaway and the incubation period. On the other hand, the model can predict the primary gas products at the time of venting based on the safety valve threshold, offering a theoretical basis for gas detection and cooling suppression during the incubation period, thereby aiding in the prevention of thermal runaway.

However, some limitations existed in this study. Firstly, a lumped model is used. While this approach conserves computational resources, it ignores the internal temperature gradients within the cell. The thermal runaway behaviours is more complex for larger-format cells with multiple jellyrolls (i.e., larger prismatic cells for energy storage systems) or blade cells with safety valves on the side. These cases require the development of three-dimensional models to describe thermal runaway evolution accurately. The CFD models will be considered and incorporated when studying the gas field after the thermal runaway. Secondly, this work simplified the effects of low ambient pressure on mass and energy loss during venting based on research findings from the literature. Although the simulation results agree well with the experimental data, a more detailed investigation is necessary to explore the assumption applicability in other thermal runaway abuse tests. Moreover, this work ignored the impact of safety pressure on the effective mass loss fraction of the electrolyte based on the literature [49]. More refined experiments are needed to observe the venting characteristics during the battery thermal runaway. Despite these limitations, the research framework proposed by this work can still enhance our understanding of thermal runaway under low ambient pressure and provide novel insights for the battery safety design.

## 4. Conclusions

This work develops a numerical model to simulate and understand the battery thermal runaway under reduced ambient pressures. The heat release from chemical reactions, gas generation, and venting process during the battery thermal runaway is incorporated and solved by the lumped model to predict the evolution of cell internal pressure and

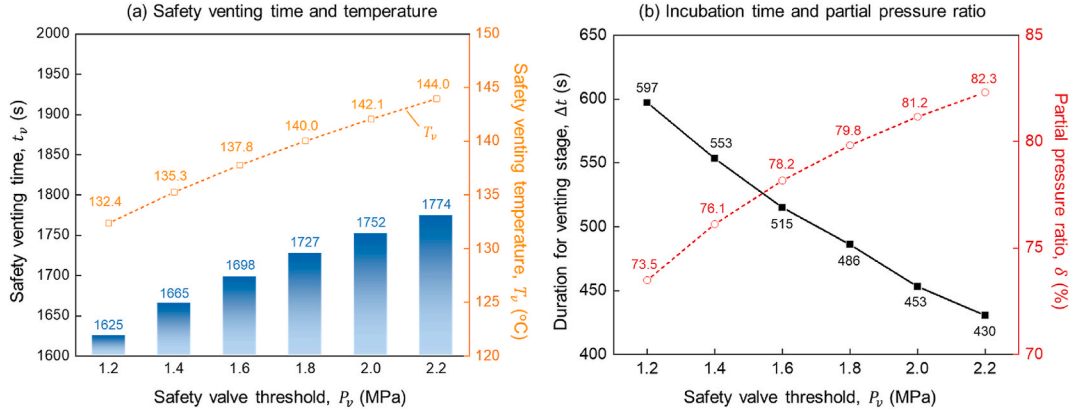


**Fig. 8.** Effect of safety valve threshold ($P_v$) on (a) safety venting time and temperature, as well as (b) incubation time and partial pressure ratio at a heating rate of 4 °C $min^{-1}$.

temperature. The model also considers the effect of ambient pressure on mass loss and energy dissipation during the venting stage. The commonly used coil heating tests are employed to determine the critical parameters for quantifying the energy loss from the cell. Based on the developed model, the impacts of ambient pressure, cell heating rate, and safety valve threshold on battery thermal failure are investigated.

Results indicate that the entire process of battery thermal failure is delineated by two critical events: safety venting and thermal runaway. Before safety venting, the rise in internal pressure is initially driven by the vaporisation of the electrolyte and gradually becomes dominated by gases produced from internal reactions. At the moment of safety venting, the partial pressure ratio for SEI decomposition gas increases from 73.5 % to 82.3 % as the safety valve threshold rises from 1.2 MPa to 2.2 MPa at a heating rate of 4 °C $min^{-1}$. After safety venting, the venting duration (or incubation period) extends by about 102 % as the heating rate decreases from 10 °C $min^{-1}$ to 4 °C $min^{-1}$ at 100 kPa. The extension of the incubation period is more pronounced under low ambient pressure, with the venting duration prolonged by 286 % at 20 kPa. In other words, thermal runaway can be significantly delayed using a slow heating rate under low ambient pressure. Finally, the implications and challenges are discussed to generalise the findings of this study, advancing our understanding of thermal runaway under low ambient pressure and offering new perspectives for improving battery safety design.

## CRediT authorship contribution statement

**Yanhui Liu:** Writing – original draft, Validation, Methodology, Investigation, Formal analysis, Data curation. **Changxiang He:** Writing – review & editing, Validation, Methodology, Investigation. **Gregory Offer:** Writing – review & editing, Resources. **Huizhi Wang:** Writing – review & editing, Supervision, Resources, Investigation. **Xinyan Huang:** Writing – review & editing, Supervision, Project administration, Investigation, Funding acquisition. **Tianshou Zhao:** Resources.

## Declaration of competing interest

The authors declare that they have no known competing financial interests or personal relationships that could have appeared to influence the work reported in this paper.

## Acknowledgements

The authors thank the support from the National Key Research and Development Program (2022YFE0207400), and China Energy Storage Alliance.

## Data availability

Data will be made available on request.

## References

[1] Y. Jin, Z. Zheng, D. Wei, X. Jiang, H. Lu, L. Sun, et al., Detection of micro-scale Li dendrite via H2 gas capture for early safety warning, Joule 4 (2020) 1714–1729.
[2] J. He, J. Meng, Y. Huang, Challenges and recent progress in fast-charging lithium-ion battery materials, J. Power Sources 570 (2023) 232965.
[3] J. Weng, Q. Huang, X. Li, G. Zhang, D. Ouyang, M. Chen, et al., Safety issue on PCM-based battery thermal management: material thermal stability and system hazard mitigation, Energy Storage Mater. 53 (2022) 580–612.
[4] L. Deguenon, D. Yamegueu, S. Moussa kadri, A. Gomna, Overcoming the challenges of integrating variable renewable energy to the grid: a comprehensive review of electrochemical battery storage systems, J. Power Sources 580 (2023) 233343.
[5] S. Xie, X. Yang, Q. Sun, Z. Wang, Y. He, Research progress and prospects on thermal safety of lithium-ion batteries in aviation low-temperature and low-pressure environments, J. Energy Storage 83 (2024) 110734.
[6] N. Williard, C. Hendricks, B. Sood, J.S. Chung, M. Pecht, Evaluation of batteries for safe air transport, Energies 9 (2016) 340.
[7] Federal Aviation Administration, Lithium Battery Incidents, 2024.
[8] LithiumSafe, Lithium Battery Fire Hazard in the Aviation Industry, 2024.
[9] C. Drew, J. Mouawad, Safety board gives new details on boeing battery fire, but not cause, N. Y. Times 7 (2013).
[10] H. Sadeghi, F. Restuccia, Pyrolysis-based modelling of 18650-type lithium-ion battery fires in thermal runaway with LCO, LFP and NMC cathodes, J. Power Sources 603 (2024) 234480.
[11] Y.S. Duh, X. Liu, X. Jiang, C.S. Kao, L. Gong, R. Shi, Thermal kinetics on exothermic reactions of a commercial LiCoO2 18650 lithium-ion battery and its components used in electric vehicles: a review, J. Energy Storage 30 (2020) 101422.
[12] S. Chen, X. Wei, G. Zhang, X. Wang, J. Zhu, X. Feng, et al., All-temperature area battery application mechanism, performance, and strategies, Innovation 4 (2023).
[13] T.T. Nguyen, S. Abada, A. Lecocq, J. Bernard, M. Petit, G. Marlair, et al., Understanding the thermal runaway of Ni-rich lithium-ion batteries, World Electr. Veh. J. 10 (2019).
[14] Q. Wang, B. Mao, S.I. Stoliarov, J. Sun, A review of lithium ion battery failure mechanisms and fire prevention strategies, Prog. Energy Combust. Sci. 73 (2019) 95–131.
[15] X. Feng, M. Ouyang, X. Liu, L. Lu, Y. Xia, X. He, Thermal runaway mechanism of lithium ion battery for electric vehicles: a review, Energy Storage Mater. 10 (2018) 246–267.
[16] R.H. Kim, D.H. Lee, Y.K. Kim, C.H. Chu, Y.G. Lee, D.K. Kim, Numerical analysis of thermal runaway process of lithium-ion batteries considering combustion, J. Energy Storage 78 (2024) 110041.
[17] Y. Wu, Z. Zeng, S. Lei, M. Liu, W. Zhong, M. Qin, et al., Passivating lithiated graphite via targeted repair of SEI to inhibit exothermic reactions in early-stage of thermal runaway for safer lithium-ion batteries, Angew. Chem. Int. Ed. 62 (2023) e202217774.
[18] Q. Wang, L. Jiang, Y. Yu, J. Sun, Progress of enhancing the safety of lithium ion battery from the electrolyte aspect, Nano Energy 55 (2019) 93–114.
[19] A.R. Baird, E.J. Archibald, K.C. Marr, O.A. Ezekoye, Explosion hazards from lithium-ion battery vent gas, J. Power Sources 446 (2020) 227257.
[20] D. Ren, X. Feng, L. Liu, H. Hsu, L. Lu, L. Wang, et al., Investigating the relationship between internal short circuit and thermal runaway of lithium-ion batteries under thermal abuse condition, Energy Storage Mater. 34 (2021) 563–573.
[21] J. Weng, D. Ouyang, Y. Liu, M. Chen, Y. Li, X. Huang, et al., Alleviation on battery thermal runaway propagation: effects of oxygen level and dilution gas, J. Power Sources 509 (2021) 230340.
[22] A. García, J. Monsalve-Serrano, R.L. Sari, S. Martinez-Boggio, Influence of environmental conditions in the battery thermal runaway process of different chemistries: thermodynamic and optical assessment, Int. J. Heat Mass Tran. 184 (2022) 122381.
[23] R. Srinivasan, M.E. Thomas, M.B. Airola, B.G. Carkhuff, L.J. Frizzell-Makowski, H. Alkandry, et al., Preventing cell-to-cell propagation of thermal runaway in lithium-ion batteries, J. Electrochem. Soc. 167 (2020) 20559.
[24] B. Gulsoy, H. Chen, C. Briggs, T.A. Vincent, J.E.H. Sansom, J. Marco, Real-time simultaneous monitoring of internal temperature and gas pressure in cylindrical cells during thermal runaway, J. Power Sources 617 (2024) 235147.
[25] J.K. Ostanek, M. Parhizi, W. Li, G. Kilaz, K.R. Crompton, CFD-based thermal abuse simulations including gas generation and venting of an 18650 Li-ion battery cell, J. Electrochem. Soc. 170 (2023) 90512.
[26] A. García, J. Monsalve-Serrano, F. de Vargas Lewiski, C. Guaraco-Figueira, Enhancing thermal runaway characterization in NMC811 lithium-ion batteries through laser-induced triggering, J. Power Sources 610 (2024) 234744.
[27] H. Wang, H. Xu, Z. Zhang, Q. Wang, C. Jin, C. Wu, et al., Fire and explosion characteristics of vent gas from lithium-ion batteries after thermal runaway: a comparative study, ETransportation 13 (2022) 100190.
[28] Y. Jin, Z. Zhao, S. Miao, Q. Wang, L. Sun, H. Lu, Explosion hazards study of grid-scale lithium-ion battery energy storage station, J. Energy Storage 42 (2021) 102987.
[29] H. Yan, O.A. Ezekoye, State of charge effects on active material elemental composition changes between pre-thermal-runaway and post-failure states for 8-1-1 nickel-manganese-cobalt 18650 cells, J. Energy Storage 63 (2023) 106974.
[30] J. Hu, T. Liu, X. Wang, Effect of discharge operation on thermal runaway incubation process of lithium-ion battery: an experimental study, Process Saf. Environ. Protect. 185 (2024) 25–35.
[31] P. Qin, J. Sun, Q. Wang, A new method to explore thermal and venting behavior of lithium-ion battery thermal runaway, J. Power Sources 486 (2021) 229357.
[32] A. García, J. Monsalve-Serrano, R. Lago Sari, S. Martinez-Boggio, An optical investigation of thermal runaway phenomenon under thermal abuse conditions, Energy Convers. Manag. 246 (2021) 114663.
[33] G. Wang, D. Kong, P. Ping, J. Wen, X. He, H. Zhao, et al., Revealing particle venting of lithium-ion batteries during thermal runaway: a multi-scale model toward multiphase process, ETransportation 16 (2023) 100237.
[34] W. Li, J. Ostanek, Heat transfer experiments and correlations for vent gases emerging from a Li-ion battery and impinging on a flat surface, Int. J. Heat Mass Tran. 200 (2023) 123516.
[35] G. Wang, D. Kong, P. Ping, X. He, H. Lv, H. Zhao, et al., Modeling venting behavior of lithium-ion batteries during thermal runaway propagation by coupling CFD and thermal resistance network, Appl. Energy 334 (2023) 120660.
[36] Y. Liu, H. Niu, Z. Li, J. Liu, C. Xu, X. Huang, Thermal runaway characteristics and failure criticality of massive ternary Li-ion battery piles in low-pressure storage and transport, Process Saf. Environ. Protect. 155 (2021) 486–497.
[37] Y. Liu, H. Niu, C. Xu, X. Huang, Thermal runaway propagation in linear battery module under low atmospheric pressure, Appl. Therm. Eng. 216 (2022) 119086.
[38] H. Wang, Z. Du, L. Liu, Z. Zhang, J. Hao, Q. Wang, et al., Study on the thermal runaway and its propagation of lithium-ion batteries under low pressure, Fire Technol. 56 (2020) 2427–2440.

[39] Y. Fu, S. Lu, L. Shi, X. Cheng, H. Zhang, Ignition and combustion characteristics of lithium ion batteries under low atmospheric pressure, Energy 161 (2018) 38–45.
[40] L. Zhang, P. Zhao, M. Xu, X. Wang, Computational identification of the safety regime of Li-ion battery thermal runaway, Appl. Energy 261 (2020) 114440.
[41] M. Parhizi, A. Jain, G. Kilaz, J.K. Ostanek, Accelerating the numerical solution of thermal runaway in Li-ion batteries, J. Power Sources 538 (2022) 231531.
[42] P.J. Bugryniec, D.J.N. Davidson, D.S.F. Brown, Advanced abuse modelling of Li-ion cells – a novel description of cell pressurisation and simmering reactions, J. Power Sources 474 (2020) 228396.
[43] R. Peng, D. Kong, P. Ping, G. Wang, X. Gao, H. Lv, et al., Thermal runaway modeling of lithium-ion batteries at different scales: recent advances and perspectives, Energy Storage Mater. 69 (2024) 103417.
[44] G. Wang, P. Ping, D. Kong, R. Peng, X. He, Y. Zhang, et al., Advances and challenges in thermal runaway modeling of lithium-ion batteries, Innovation (2024) 100624.
[45] D. Mishra, K. Shah, A. Jain, Investigation of the impact of flow of vented gas on propagation of thermal runaway in a Li-ion battery pack, J. Electrochem. Soc. 168 (2021) 60555.
[46] B. Mao, C. Fear, H. Chen, H. Zhou, C. Zhao, P.P. Mukherjee, et al., Experimental and modeling investigation on the gas generation dynamics of lithium-ion batteries during thermal runaway, ETransportation 15 (2023) 100212.
[47] P.T. Coman, S. Rayman, R.E. White, A lumped model of venting during thermal runaway in a cylindrical Lithium Cobalt Oxide lithium-ion cell, J. Power Sources 307 (2016) 56–62.
[48] P.T. Coman, S. Mátéfi-Tempfli, C.T. Veje, R.E. White, Modeling vaporization, gas generation and venting in Li-ion battery cells with a dimethyl carbonate electrolyte, J. Electrochem. Soc. 164 (2017) A1858.
[49] J.K. Ostanek, W. Li, P.P. Mukherjee, K.R. Crompton, C. Hacker, Simulating onset and evolution of thermal runaway in Li-ion cells using a coupled thermal and venting model, Appl. Energy 268 (2020) 114972.
[50] C.X. He, Q.L. Yue, Q. Chen, T.S. Zhao, Modeling thermal runaway of lithium-ion batteries with a venting process, Appl. Energy 327 (2022) 120110.
[51] J. Kim, A. Mallarapu, D.P. Finegan, S. Santhanagopalan, Modeling cell venting and gas-phase reactions in 18650 lithium ion batteries during thermal runaway, J. Power Sources 489 (2021) 229496.
[52] D. Kong, G. Wang, P. Ping, J. Wen, A coupled conjugate heat transfer and CFD model for the thermal runaway evolution and jet fire of 18650 lithium-ion battery under thermal abuse, ETransportation 12 (2022) 100157.
[53] P. Zhang, J. Lu, K. Yang, H. Chen, Y. Huang, A 3D simulation model of thermal runaway in Li-ion batteries coupled particles ejection and jet flow, J. Power Sources 580 (2023) 233357.
[54] A. Gil, C. Micó, J. Marco-Gimeno, M.C. Espín, Numerical approach for the characterization of the venting process of cylindrical cells under thermal runaway conditions, SAE Tech. Pap. (2024).
[55] W. Huang, X. Feng, Y. Pan, C. Jin, J. Sun, J. Yao, et al., Early warning of battery failure based on venting signal, J. Energy Storage 59 (2023) 106536.
[56] A.W. Golubkov, D. Fuchs, J. Wagner, H. Wiltsche, C. Stangl, G. Fauler, et al., Thermal-runaway experiments on consumer Li-ion batteries with metal-oxide and olivin-type cathodes, RSC Adv. 4 (2014) 3633–3642.
[57] L. Liu, C. Lin, B. Fan, F. Wang, L. Lao, P. Yang, A new method to determine the heating power of ternary cylindrical lithium ion batteries with highly repeatable thermal runaway test characteristics, J. Power Sources 472 (2020) 228503.
[58] J.K. Ostanek, N.R. Baehl, M. Parhizi, J.A. Jeevarajan, Hot gas impingement and radiation on neighboring surfaces from venting and combustion in a package of 18650 cells, J. Power Sources Adv. 28 (2024) 100150.
[59] T.D. Hatchard, D.D. MacNeil, A. Basu, J.R. Dahn, Thermal model of cylindrical and prismatic lithium-ion cells, J. Electrochem. Soc. 148 (2001) A755.
[60] D. Ren, X. Liu, X. Feng, L. Lu, M. Ouyang, J. Li, et al., Model-based thermal runaway prediction of lithium-ion batteries from kinetics analysis of cell components, Appl. Energy 228 (2018) 633–644.
[61] Y. Liu, L. Zhang, X. Huang, M. Hao, X. Huang, Laser-induced thermal runaway dynamics of cylindrical lithium-ion battery, J. Energy Storage 86 (2024) 111337.
[62] E.W. Lemmon, M.L. Huber, M.O. McLinden, NIST standard reference database 23, Ref. Fluid Therm. Transport. Proper. (REFPROP) 9 (2010). Version.
[63] H. Zhou, C. Fear, M. Parekh, F. Gray, J. Fleetwood, T. Adams, et al., The role of separator thermal stability in safety characteristics of lithium-ion batteries, J. Electrochem. Soc. 169 (2022) 90521.
[64] T. Cai, V. Tran, A.G. Stefanopoulou, J.B. Siegel, Modeling Li-ion battery first venting events before thermal runaway, IFAC-PapersOnLine 54 (2021) 528–533.
[65] Y. Zheng, Z. Shi, D. Ren, J. Chen, X. Liu, X. Feng, et al., In-depth investigation of the exothermic reactions between lithiated graphite and electrolyte in lithium-ion battery, J. Energy Chem. 69 (2022) 593–600.
[66] A.O. Said, C. Lee, S.I. Stoliarov, Experimental investigation of cascading failure in 18650 lithium ion cell arrays: impact of cathode chemistry, J. Power Sources 446 (2020) 227347.
[67] Q. Sun, H. Liu, M. Zhi, C. Zhao, J. Jia, P. Lv, et al., Lithium-Ion Battery Thermal Runaway Propagation Characteristics under 20 kPa with Different Airflow Rates, Fire Technology, 2022.
[68] X. Feng, L. Lu, M. Ouyang, J. Li, X. He, A 3D thermal runaway propagation model for a large format lithium ion battery module, Energy 115 (2016) 194–208.
[69] H. Wang, B. Liu, C. Xu, C. Jin, K. Li, Z. Du, et al., Dynamic thermophysical modeling of thermal runaway propagation and parametric sensitivity analysis for large format lithium-ion battery modules, J. Power Sources 520 (2022) 230724.
[70] X. Lai, S. Wang, H. Wang, Y. Zheng, X. Feng, Investigation of thermal runaway propagation characteristics of lithium-ion battery modules under different trigger modes, Int. J. Heat Mass Tran. 171 (2021) 121080.
[71] J. Weng, C. Xiao, X. Yang, D. Ouyang, M. Chen, G. Zhang, et al., An energy-saving battery thermal management strategy coupling tubular phase-change-material with dynamic liquid cooling under different ambient temperatures, Renew. Energy 195 (2022) 918–930.
[72] Y. Liu, G. Aldan, X. Huang, M. Hao, Single-phase static immersion cooling for cylindrical lithium-ion battery module, Applied Thermal Engineering 233 (2023) 121184.